

Strain-engineered oxygen vacancies in CaMnO_3 thin films

Ravini U. Chandrasena,^{1,2} Weibing Yang,^{1,2} Qingyu Lei,^{1,2} Mario U. Delgado-Jaime,³ Kanishka D. Wijesekara,^{1,2} Maryam Golalikhani,^{1,2} Bruce Davidson,¹ Elke Arenholz,⁴ Keisuke Kobayashi,⁵ Masaaki Kobata,⁵ Frank M. F. de Groot,³ Ulrich Aschauer,^{6,7} Nicola A. Spaldin,⁶ Xiaoxing X. Xi,^{1,2} and Alexander X. Gray^{1,2,*}

¹ Department of Physics, Temple University, 1925 North 12th Street, Philadelphia, Pennsylvania 19122, USA

² Temple Materials Institute, Temple University, 1925 North 12th Street, Philadelphia, Pennsylvania 19122, USA

³ Inorganic Chemistry & Catalysis, Debye Institute for Nanomaterials Science, Utrecht University, Universiteitsweg 99, Utrecht 3584 CG, The Netherlands

⁴ Advanced Light Source, Lawrence Berkeley National Laboratory, One Cyclotron Road, Berkeley, California 94720, USA

⁵ Materials Sciences Research Center, Japan Atomic Energy Agency, 1-1-1 Kouto, Sayo-cho, Hyogo, 679-5148, Japan

⁶ Materials Theory, ETH Zurich, Wolfgang-Pauli-Strasse 27, CH-8093 Zürich, Switzerland

⁷ Department of Chemistry and Biochemistry, University of Bern, Freiestrasse 3, CH-3012 Bern, Switzerland

* e-mail: axgray@temple.edu

Abstract

We demonstrate a novel pathway to control and stabilize oxygen vacancies in complex transition-metal oxide thin films. Using atomic layer-by-layer pulsed laser deposition (PLD) from two separate targets, we synthesize high-quality single-crystalline CaMnO_3 films with systematically varying oxygen vacancy defect formation energies as controlled by coherent tensile strain. The systematic increase of the oxygen vacancy content in CaMnO_3 as a function of applied in-plane strain is observed and confirmed experimentally using high-resolution soft x-ray absorption spectroscopy (XAS) in conjunction with bulk-sensitive hard x-ray photoemission spectroscopy (HAXPES). The relevant defect states in the densities of states are identified and the vacancy content in the films quantified using the combination of first-principles theory and core-hole multiplet calculations with holistic fitting. Our findings open up a promising avenue for designing and controlling new ionically-active properties and functionalities of complex transition-metal oxides via strain-induced oxygen-vacancy formation and ordering.

Keywords

strongly-correlated oxides, strain engineering, oxygen vacancies, x-ray spectroscopy

Text

Dynamic control of ionic defects in transition-metal oxides and their interfaces is considered to be an exciting new avenue towards creating materials with novel electronic, magnetic and structural properties ^{1,2}. Such an approach for materials design, strongly reminiscent of the principles that enable modern semiconductor technology, has tremendous potential due to the fact that very small changes in the concentrations of defects such as oxygen vacancies can lead to dramatic changes in the materials' properties and function, such as conductivity ³ and magnetism ⁴. Thus, our ability to tailor and fine-tune the densities and concentration profiles of such functional defects largely determines the full range of novel phenomena and functionalities accessible in such systems.

Coherent epitaxial strain has been widely utilized as a tuning knob to control key functional properties in transition-metal oxides. Recent examples of such strain-functionality coupling include the control of metal-to-insulator transition temperature in VO₂ ⁵ and the insulator-to-superconductor transition temperature in La_{1.9}Sr_{0.1}CuO₄ ⁶. Going beyond the ability to effectively manipulate already existing physical properties of a given material, strain has also been shown to invoke entirely new exotic ground states such as ferroelectricity in SrTiO₃ and increased ferroelectric polarization in BaTiO₃, consistent with theoretical predictions⁷⁻⁹.

The antiferromagnetic Mott insulator CaMnO₃ is a well-established example of a complex transition-metal oxide in which electronic and magnetic properties can be manipulated via strain, heteroengineering and external stimuli ¹⁰⁻¹⁴. A recent theoretical study suggests that, in addition to directly affecting internal bond lengths and oxygen octahedral rotations, coherent epitaxial strain can facilitate spontaneous formation of oxygen vacancies and even influence defect-site preference leading to vacancy ordering in CaMnO₃ and similar materials ^{15, 16}. This prediction opens the door

for exploring and controlling new properties and functionalities stemming from ionic activity. Thus, a clear understanding of the energetics and strain-control of such defects is crucial for achieving technical feasibility and efficient performance of future electronic devices relying on these properties.

Here we use a combination of atomic layer-by-layer pulsed laser deposition (PLD) from two separate targets, bulk-sensitive x-ray spectroscopies (XAS and HAXPES), and a combination of theoretical methods to show a direct relationship between applied coherent epitaxial strain and oxygen vacancy concentration in ultrathin single-crystalline CaMnO_3 films. Spectroscopic fingerprints of the defect-induced electronic states are identified and analyzed. It is furthermore revealed that, due to their high mobility^{17, 18}, the vacancies partially diffuse out of the film when exposed to ambient atmosphere, thus necessitating an in-situ-grown capping layer to preserve the original strain-induced oxygen-vacancy content. This underlines the importance of bulk-sensitive x-ray techniques, capable of probing buried layers and interfaces, for the understanding of the electronic properties of strain-engineered thin films.

Two identical sets of ultrathin (10 unit cells) single-crystalline CaMnO_3 films were synthesized using atomic layer-by-layer PLD¹⁹ on three different single-crystalline substrates inducing coherent in-plane tensile strain varying from +0.8% to +4% (see Supplementary Information for details). Coherent epitaxy at such high strain levels is made possible by atomic layer-by-layer synthesis via alternating ablation of two separate constituent oxide targets (MnO_2 and CaO)¹⁹. A thicker (80 unit cells) bulk-like CaMnO_3 film was grown on a SrTiO_3 substrate as a fully-relaxed (0% strain) reference sample. To investigate the effect of ambient atmospheric exposure on the oxygen-vacancy content, one complete set of films was capped with a 3 nm-thick Pt capping layer in-situ and the other identical set synthesized during the same run was left

exposed. Quality, crystallinity and thickness of the films was verified using x-ray diffraction (XRD) and reflection high-energy electron diffraction (RHEED) measurements (see Fig. S1 and accompanying discussion in the Supplementary Information). In addition, an exhaustive characterization of such coherently-strained CaMnO_3 films via XRD, x-ray reflectivity and atomic force microscopy was carried out by us in a prior study ²⁰, confirming crystallinity, tensile strain values, phase purity and coherence.

Soft x-ray XAS measurements at the Mn $L_{2,3}$ and O K absorption thresholds were carried out at the elliptically polarized undulator beamline 4.0.2 of the Advanced Light Source using the Vector Magnet endstation ²¹. The average probing depth in the total electron yield XAS detection mode was estimated to be approximately 5 nm, providing optimal bulk-sensitivity to probe the buried CaMnO_3 layer underneath the 3 nm-thick Pt cap. Measurements were carried out at several locations on the sample, to exclude the possibility of x-ray sample damage.

Complementary core-level HAXPES measurements of the Mn $3s$ multiplet-split spectra were carried out using a focused monochromated Cr $K\alpha$ x-ray source integrated with a VG Scienta R4000 hemispherical analyzer ²² equipped with an additional wide acceptance objective lens. At the Cr $K\alpha$ excitation energy of 5.4 keV, the inelastic mean-free paths (IMFP) of the photoemitted Mn $3s$ electrons in CaMnO_3 and Pt are estimated to be 8.0 nm and 4.4 nm respectively ²³. Therefore, HAXPES has an advantage over traditional XPS of being able to probe these electronic states in a buried layer and through the 3 nm-thick Pt cap.

Observed strain-dependent changes in the electronic structure of buried CaMnO_3 films strongly suggest systematic variation in the Mn valence state due to oxygen vacancy formation with increased tensile strain,¹⁵ as described in the following paragraphs.

We first discuss the changes in the Mn valence state and conduction-band orbital energetics as a function of in-plane strain. The excess charge associated with a neutral oxygen vacancy in CaMnO_3 is accommodated in the lattice via the reduction of two Mn^{4+} to Mn^{3+} on sites adjacent to the vacancy²⁴. Tensile strain thus lowers the oxygen vacancy formation energy since the expanded lattice facilitates the increase in ionic radius associated with these reduction reactions¹⁵.

In Figure 1a, we plot the XAS spectra of the Mn $L_{2,3}$ edges for the four Pt-capped CaMnO_3 films exhibiting tensile strain ranging from 0% (fully relaxed film) to 4%, as grown on an $(\text{LaAlO}_3)_{0.3}(\text{Sr}_2\text{AlTaO}_6)_{0.7}$ (LSAT) substrate. XAS at the $L_{2,3}$ edges has been used routinely for the analysis of the transition-metal valence states in oxides^{25, 26}. Spin-orbit coupling splits the transition-metal $L_{2,3}$ edge into two components, L_2 and L_3 , corresponding to the $2p_{1/2} \rightarrow 3d$ and $2p_{3/2} \rightarrow 3d$ transitions respectively^{25, 26}. The most striking evidence of the changes in the Mn valence state towards Mn^{3+} is observed with the systematic shift of the L_2 and L_3 spectral weights towards lower photon energies²⁶⁻²⁹ as a function of increasing strain. The spectral shift is due to changes in the electrostatic energy at the Mn site driven by the decrease in the $3d$ count, which leads to shifts of both the core level and the final-state wavefunctions^{27, 30}. The observed total chemical shift of approximately 0.7 eV is immediately obvious to the eye for the L_2 edge (see Figure 1a) and can be verified for the L_3 edge via appropriate peak fitting, which is necessary due to the more complex structure of the excitonic region of the L_3 edge.

In addition to the abovementioned chemical shift, increase of the Mn^{3+} content with increased tensile strain is evidenced by the systematic increase in spectral weight of the feature at the photon energy of 640.3 eV, shown in the outset of Figure 1a, and identified in prior studies as the signature of the Mn^{3+} high-spin valence state^{31, 32}. Ratios of the spectral weight of the Mn^{3+} peak to the total spectral weight of the L_3 edge, obtained via background subtraction and peak-

fitting, are plotted in Figure 1b and exhibit monotonic increase as a function of strain. Corresponding systematic changes in the strain-dependent oxygen vacancy formation energies, calculated using density functional theory as in Ref.¹⁵, are plotted on the left axis and shown by green symbols.

Another indicator of the increase of the Mn^{3+} content, the L_3/L_2 intensity ratio which is highly sensitive to the valence state of Mn ions^{33, 34}, is calculated and plotted in Figure 1b as a function of tensile strain. For the fully-relaxed bulk-like CaMnO_3 film, the ratio is the lowest of the series (close to 2), consistent with the d^3 configuration of the predominant Mn^{4+} ion³³. The ratio grows as a function of increased tensile strain (see Figure 1b), which strongly suggests an increase in the concentration of Mn^{3+} ions with d^4 configuration³³. Consistent with the Mn^{3+} peak intensities, the L_3/L_2 ratios are also correlated to the calculated oxygen vacancy formation energies for the respective strain values.

To determine the Mn^{3+} and Mn^{4+} ionic content in each sample, we simultaneously and self-consistently fit our experimental data using spectra calculated for the respective Mn species via multiplet simulations^{35, 36}. In our model, the corresponding reductions of Slater integrals (which account for covalency) and the crystal-field parameters, in combination with Lorentzian and Gaussian broadenings, are all treated as the fit parameters. The edge jumps, modeled as cumulative pseudo-Voigt functions, and background functions are included for each data set. The resultant reference spectra for the Mn^{3+} and Mn^{4+} species are applied simultaneously to all data sets, with a common energy shift and varying scaling factors to account for the differences in composition between different samples. The fitting is performed using the Blueprint XAS package^{35, 36}, which enables calculations of multiple fits from multiple reduced-bias starting points, making it possible to evaluate uncertainties in the fit parameters as well as the derived quantities. Figure 2a shows

the resultant fits with the two optimized reference spectra calculated for the Mn^{3+} and Mn^{4+} species acting on all four datasets. Figure 2b shows the resultant compositions and their corresponding uncertainties. Other relevant parameters obtained from the fitting are tabulated in Table S1 of the Supplementary Information.

Similar measurements and spectroscopic analysis carried out for the identical set of CaMnO_3 films grown during the same run but without the protective Pt capping layer suggests that the vacancies partially diffuse out of the film when exposed to ambient atmosphere (see Figure S1 in the Supporting Information). The uncapped films are still subjected to the same systematically-varying substrate-induced coherent tensile strain as the capped samples, however, the spectral shapes for the strained films on LaSrAlO_4 and LaAlO_3 substrates (0.8% and 1.9% strain, respectively) look virtually indistinguishable from that for the bulk-like CaMnO_3 film with predominantly Mn^{4+} valence (black spectrum). Significant spectral shape changes, fully consistent with the increase in the Mn^{3+} ion concentration as described above, are only observed for the maximally-strained film on the LSAT substrate (green spectrum), but to a lesser extent when compared to the similar capped sample (see Figure 1a). Our observations confirm the prediction that equilibrium room-temperature oxygen vacancy concentrations are low and that oxygen vacancies remain mobile even at low temperatures and can diffuse out of the film when exposed to ambient atmosphere¹⁵. We emphasize that, while strain strongly enhances the oxygen vacancy concentration (by about an order of magnitude at 650 K and a factor of five at 950 K, the enhancement actually being stronger at low temperature), the small absolute oxygen vacancy concentration at room temperature makes the change in Mn^{3+} concentration undetectable by XAS. Using the Pt capping layer, we block oxygen uptake by the film and preserve the increased high-temperature oxygen vacancy concentration that is metastable at room temperature. This

furthermore underlines the importance of non-destructive bulk-sensitive x-ray techniques, such as XAS and HAXPES, capable of probing electronic properties of films that are buried underneath protective capping layers.

Figure 3 shows bulk-sensitive HAXPES measurements of the Mn 3s multiplet-split spectra for the Pt-capped coherently-strained CaMnO_3 films. In 3d transition metals, the 3s core-level splitting arises due to the exchange coupling interaction between the 3s core-hole and 3d electrons and due to the intrashell 3d charge transfer process^{37, 38}. As the valence state of the Mn ion tends to decrease, the energy splitting between the two Mn 3s multiplet components increases^{38, 39}. Therefore, the 3s splitting is highly sensitive to the changes in the valence state of Mn ions and, in fact, has been used in numerous prior studies to determine the Mn valence state³⁹. Self-consistent Shirley-background subtraction and peak-fitting reveals that the Mn 3s splitting increases systematically with in-plane tensile strain (see Figure 3b). The low value of 4.49 eV is observed for the fully-relaxed bulk-like film (see Figure 3a), consistent with the prior studies and indicating predominantly Mn^{4+} ion content⁴⁰⁻⁴². The high value of 4.64 eV is observed for the maximally-strained (+4.0% tensile) film on the LSAT substrate (see Figure 3a), indicating a significant contribution of the lower-valent Mn^{3+} ions, consistent with the XAS results. By assuming a homogeneous linear combination of the Mn^{3+} and Mn^{4+} concentrations in the film, as a first-order approximation we estimate that the maximally-strained CaMnO_3 film on the LSAT substrate contains up to 20% more Mn^{3+} ions compared to the fully-relaxed film, which is in excellent agreement with the results of the holistic fitting of the XAS spectra (see Figure 2b).

Lastly, we utilized the combination of high-resolution XAS at the O K absorption edge and first-principle density-of-states calculations to probe the electronic defect states in the conduction band of CaMnO_3 . The O K edge XAS probes the O 2p-projected unoccupied density of states

1
2
3 resulting from dipole-allowed x-ray transitions from the $1s$ core shell^{43,44}. It is well known that
4
5 the few-eV-wide region immediately above the absorption threshold (pre-edge) provides access to
6
7 the relevant states in the unoccupied CaMnO_3 conduction band via O $2p$ - Mn $3d$ orbital
8
9 hybridization^{43,44}. Therefore, since these $2p$ - $3d$ hybridized states are highly sensitive to the oxygen
10
11 octahedral distortions as well as to the presence of oxygen vacancies, O K pre-edge XAS can be
12
13 effectively used to detect electronic states induced by such defects⁴⁵ and to analyze electronic-
14
15 structural changes resulting in vacancy formation⁴⁵. While ground-state density-of-states
16
17 calculations do not allow us to directly predict spectral shapes, we can tie the existence of spectral
18
19 features to predicted changes in the energies of states.
20
21
22
23

24 In Figure 4a we plot the O K pre-edge XAS spectra for the same set of coherently-strained
25
26 Pt-capped CaMnO_3 films. The most significant strain-dependent modification of the line shape is
27
28 observed as a feature (D) on the higher-energy side of the pre-edge peak (centered at 530.5 eV)
29
30 growing systematically with increasing strain. Based on first-principles calculations (see
31
32 Supplementary Information for details) of the O $2p$ -projected density of states (pDOS) shown for
33
34 the highest (+4.0%, with oxygen vacancy) and lowest (0.0%, without oxygen vacancy) strain states
35
36 in Figure 4b, we can assign this feature to the emerging defect state (D'). Similarly to the defect
37
38 state in the band gap about 0.5 eV below the conduction-band edge¹⁵, which results from a
39
40 lowering in energy of hybridized majority-spin Mn e_g - O $2p$ states adjacent to a formed vacancy,
41
42 this state (D') results from an energy lowering of the minority-spin Mn e_g - O $2p$ states. Moreover,
43
44 we can associate the observed shift of the peak (C) at 4% strain with an upwards shift of the
45
46 hybridized minority-spin Mn t_{2g} - O $2p$ states with increasing strain (C').
47
48
49
50
51
52

53 In summary, we experimentally varied the oxygen vacancy defect formation energies in
54
55 strongly-correlated oxide CaMnO_3 by engineering ultrathin coherently-strained single-crystalline
56
57
58
59
60

1
2
3 films via atomic layer-by-layer PLD from two separate targets. Oxygen vacancy content was
4
5 stabilized by protecting the surfaces of the films with thin Pt layers in-situ. By utilizing bulk-
6
7 sensitive x-ray techniques, such as high-resolution XAS and HAXPES, as well as first-principles
8
9 theory, we probed the electronic-structural changes related to the defect formation in CaMnO_3 and
10
11 established a direct link between the coherent in-plane strain and the oxygen-vacancy content. Our
12
13 results provide a new recipe for designing strongly-correlated transition-metal oxides with tunable
14
15 ionic defect content.
16
17
18
19
20
21
22
23

24 **Supporting Information**
25

26
27 Supporting information accompanies this paper and is available free of charge via the internet at
28
29 <http://pubs.acs.org/>. It includes Sample synthesis and characterization, Calculations, XAS of
30
31 uncapped CaMnO_3 films and parameters obtained for multiplet simulations.
32
33

34 Notes:
35

36 The authors declare no competing financial interests.
37

38 Correspondence and requests for materials should be addressed to A.X.G.
39
40
41
42
43
44
45
46
47
48
49
50
51
52
53
54
55
56
57
58
59
60

Acknowledgements

A.X.G, R.U.C. and W.Y. acknowledge support from the U.S. Army Research Office, under Grant No. W911NF-15-1-0181. The sample preparation by atomic layer-by-layer PLD was supported by the U.S. Department of Energy, Office of Science, under Grant No. DE-SC0004764 (Q. Y. L. and X. X. X.). Part of this work was financially supported by the ETH Zürich and by the ERC Advanced Grant program, No. 291151. Computer resources were provided by the ETH Zürich (Euler cluster) and the Swiss Supercomputing Center (CSCS) under project s624. M.U.D.J. and F.M.F.d.G. are thankful to the European research Council (ERC) for their support under advanced grant XRAYonACTIVE (No. 340279). The Advanced Light Source is supported by the Director, Office of Science, Office of Basic Energy Sciences, US Department of Energy under Contract No. DE-AC02-05CH11231.

References

1. Kalinin, S. V.; Spaldin, N. A. *Science* **2013**, 341, 858-859.
2. Jeong, J.; Aetukuri, N.; Graf, T.; Schladt, T. D.; Samant, M. G.; Parkin, S. S. P. *Science* **2013**, 339, 1402-1405.
3. Veal, B. W.; Kim, S. K.; Zapol, P.; Iddir, H.; Baldo, P. M.; Eastman, J. A. *Nat. Commun.* **2016**, 7, 11892.
4. Rodríguez Torres, C. E.; Pasquevich, G. A.; Zélis, P. M.; Golmar, F.; Heluani, S. P.; Nayak, S. K.; Adeagbo, W. A.; Hergert, W.; Hoffmann, M.; Ernst, A.; Esquinazi, P.; Stewart, S. J. *Phys. Rev. B* **2014**, 89, 104411.
5. Aetukuri, N. B.; Gray, A. X.; Drouard, M.; Cossale, M.; Gao, L.; Reid, A. H.; Kukreja, R.; Ohldag, H.; Jenkins, C. A.; Arenholz, E.; Roche, K. P.; Durr, H. A.; Samant, M. G.; Parkin, S. S. P. *Nat. Phys.* **2013**, 9, 661-666.
6. Locquet, J. P.; Perret, J.; Fompeyrine, J.; Machler, E.; Seo, J. W.; Van Tendeloo, G. *Nature* **1998**, 394, 453-456.
7. Choi, K. J.; Biegalski, M.; Li, Y. L.; Sharan, A.; Schubert, J.; Uecker, R.; Reiche, P.; Chen, Y. B.; Pan, X. Q.; Gopalan, V.; Chen, L.-Q.; Schlom, D. G.; Eom, C. B. *Science* **2004**, 306, 1005-1009.
8. Haeni, J. H.; Irvin, P.; Chang, W.; Uecker, R.; Reiche, P.; Li, Y. L.; Choudhury, S.; Tian, W.; Hawley, M. E.; Craigo, B.; Tagantsev, A. K.; Pan, X. Q.; Streiffer, S. K.; Chen, L. Q.; Kirchoefer, S. W.; Levy, J.; Schlom, D. G. *Nature* **2004**, 430, 758-761.
9. Pertsev, N. A.; Tagantsev, A. K.; Setter, N. *Phys. Rev. B* **2000**, 61, R825-R829.
10. Takahashi, K. S.; Kawasaki, M.; Tokura, Y. *Appl. Phys. Lett.* **2001**, 79, 1324-1326.
11. Bhattacharjee, S.; Bousquet, E.; Ghosez, P. *Phys. Rev. Lett.* **2009**, 102, 117602.
12. Hongwei, W.; Lixin, H.; Xifan, W. *EPL (Europhysics Letters)* **2012**, 100, 17005.
13. Yamada, H.; Marinova, M.; Altuntas, P.; Crassous, A.; Bégon-Lours, L.; Fusil, S.; Jacquet, E.; Garcia, V.; Bouzehouane, K.; Gloter, A.; Villegas, J. E.; Barthélémy, A.; Bibes, M. *Sci. Rep.* **2013**, 3, 2834.
14. Grutter, A. J.; Kirby, B. J.; Gray, M. T.; Flint, C. L.; Alaan, U. S.; Suzuki, Y.; Borchers, J. A. *Phys. Rev. Lett.* **2015**, 115, 047601.
15. Aschauer, U.; Pfenninger, R.; Selbach, S. M.; Grande, T.; Spaldin, N. A. *Phys. Rev. B* **2013**, 88, 054111.
16. Becher, C.; Maurel, L.; Aschauer, U.; Lilienblum, M.; Magén, C.; Meier, D.; Langenberg, E.; Trassin, M.; Blasco, J.; Krug, I. P.; Algarabel, P. A.; Spaldin, N. A.; Pardo, J. A.; Fiebig, M. *Nat. Nano* **2015**, 10, 661-665.
17. Kubicek, M.; Cai, Z.; Ma, W.; Yildiz, B.; Hutter, H.; Fleig, J. *ACS Nano* **2013**, 7, 3276-3286.
18. Petrie, J. R.; Mitra, C.; Jeen, H.; Choi, W. S.; Meyer, T. L.; Reboredo, F. A.; Freeland, J. W.; Eres, G.; Lee, H. N. *Adv. Funct. Mater.* **2016**, 26, 1564-1570.
19. Lei, Q.; Golalikhani, M.; Davidson, B. A.; Liu, G.; Schlom, D. G.; Qiao Qiao; Zhu, Y.; Chandrasena, R. U.; Yang, W.; Gray, A. X.; Arenholz, E.; Farrar, A. K.; Tenne, D. A.; Hu, M.; Guo, J.; Singh, R. K.; Xi, X. X. *arXiv preprint arXiv:1610.06885* **2016**.
20. Imbrenda, D.; Yang, D.; Wang, H.; Akbashev, A. R.; Kasaei, L.; Davidson, B. A.; Wu, X.; Xi, X.; Spanier, J. E. *Appl. Phys. Lett.* **2016**, 108, 082902.
21. Young, A. T.; Arenholz, E.; Feng, J.; Padmore, H.; Marks, S.; Schlueter, R.; Hoyer, E.; Kelez, N.; Steier, C. *Surf. Rev. Lett.* **2002**, 09, 549-554.
22. Kobayashi, K.; Kobata, M.; Iwai, H. *J. Electron. Spectrosc.* **2013**, 190, Part B, 210-221.

23. Tanuma, S.; Powell, C. J.; Penn, D. R. *Surf. Interface Anal.* **2011**, 43, 689-713.
24. Zeng, Z.; Greenblatt, M.; Croft, M. *Phys. Rev. B* **1999**, 59, 8784-8788.
25. Cramer, S. P.; DeGroot, F. M. F.; Ma, Y.; Chen, C. T.; Sette, F.; Kipke, C. A.; Eichhorn, D. M.; Chan, M. K.; Armstrong, W. H. *J. Am. Chem. Soc.* **1991**, 113, 7937-7940.
26. Qiao, R.; Chin, T.; Harris, S. J.; Yan, S.; Yang, W. *Curr. Appl. Phys.* **2013**, 13, 544-548.
27. Abbate, M.; de Groot, F. M. F.; Fuggle, J. C.; Fujimori, A.; Strebel, O.; Lopez, F.; Domke, M.; Kaindl, G.; Sawatzky, G. A.; Takano, M.; Takeda, Y.; Eisaki, H.; Uchida, S. *Phys. Rev. B* **1992**, 46, 4511-4519.
28. de Groot, F. M. F. *J. Electron. Spectrosc.* **1994**, 67, 529-622.
29. Mierwaldt, D.; Mildner, S.; Arrigo, R.; Knop-Gericke, A.; Franke, E.; Blumenstein, A.; Hoffmann, J.; Jooss, C. *Catalysts* **2014**, 4, 129.
30. Belli, M.; Scafati, A.; Bianconi, A.; Mobilio, S.; Palladino, L.; Reale, A.; Burattini, E. *Solid State Commun.* **1980**, 35, 355-361.
31. Aruta, C.; Balestrino, G.; Tebano, A.; Ghiringhelli, G.; Brookes, N. B. *Europhys. Lett.* **2007**, 80, 37003.
32. Toulemonde, O.; Studer, F.; Llobet, A.; Ranno, L.; Maignan, A.; Pollert, E.; Nevriya, M.; Pellegrin, E.; Brooks, N. B.; Goedkoop, J. *J. Magn. Magn. Mater.* **1998**, 190, 307-317.
33. Varela, M.; Oxley, M. P.; Luo, W.; Tao, J.; Watanabe, M.; Lupini, A. R.; Pantelides, S. T.; Pennycook, S. J. *Phys. Rev. B* **2009**, 79, 085117.
34. Kurata, H.; Colliex, C. *Phys. Rev. B* **1993**, 48, 2102-2108.
35. Delgado-Jaime, M. U.; Kennepohl, P. *J. Synchrotron Radiat* **2010**, 17, 119-128.
36. Delgado-Jaime, M. U.; Mewis, C. P.; Kennepohl, P. *J. Synchrotron Radiat* **2010**, 17, 132-137.
37. Fadley, C. S.; Shirley, D. A. *Phys. Rev. A* **1970**, 2, 1109-1120.
38. Galakhov, V. R.; Demeter, M.; Bartkowski, S.; Neumann, M.; Ovechkina, N. A.; Kurmaev, E. Z.; Lobachevskaya, N. I.; Mukovskii, Y. M.; Mitchell, J.; Ederer, D. L. *Phys. Rev. B* **2002**, 65, 113102.
39. Beyreuther, E.; Grafström, S.; Eng, L. M.; Thiele, C.; Dörr, K. *Phys. Rev. B* **2006**, 73, 155425.
40. Ning, X.; Wang, Z.; Zhang, Z. *Sci. Rep.* **2015**, 5, 8460.
41. Ning, X. K.; Wang, Z. J.; Chen, Y. N.; Zhang, Z. D. *Nanoscale* **2015**, 7, 20635-20641.
42. Wu, Q.-H.; Liu, M.; Jaegermann, W. *Mater. Lett.* **2005**, 59, 1980-1983.
43. de Groot, F. M. F.; Grioni, M.; Fuggle, J. C.; Ghijsen, J.; Sawatzky, G. A.; Petersen, H. *Phys. Rev. B* **1989**, 40, 5715-5723.
44. Suntivich, J.; Hong, W. T.; Lee, Y.-L.; Rondinelli, J. M.; Yang, W.; Goodenough, J. B.; Dabrowski, B.; Freeland, J. W.; Shao-Horn, Y. *J. Phys. Chem. C* **2014**, 118, 1856-1863.
45. Abbate, M.; Zampieri, G.; Prado, F.; Caneiro, A.; Gonzalez-Calbet, J. M.; Vallet-Regi, M. *Phys. Rev. B* **2002**, 65, 155101.
46. Ghiasi, M.; Delgado-Jaime, M. U.; Malekzadeh, A.; Wang, R.-P.; Miedema, P. S.; Beye, M.; de Groot, F. M. F. *J. Phys. Chem. C* **2016**, 120, 8167-8174.

Figures and Legends

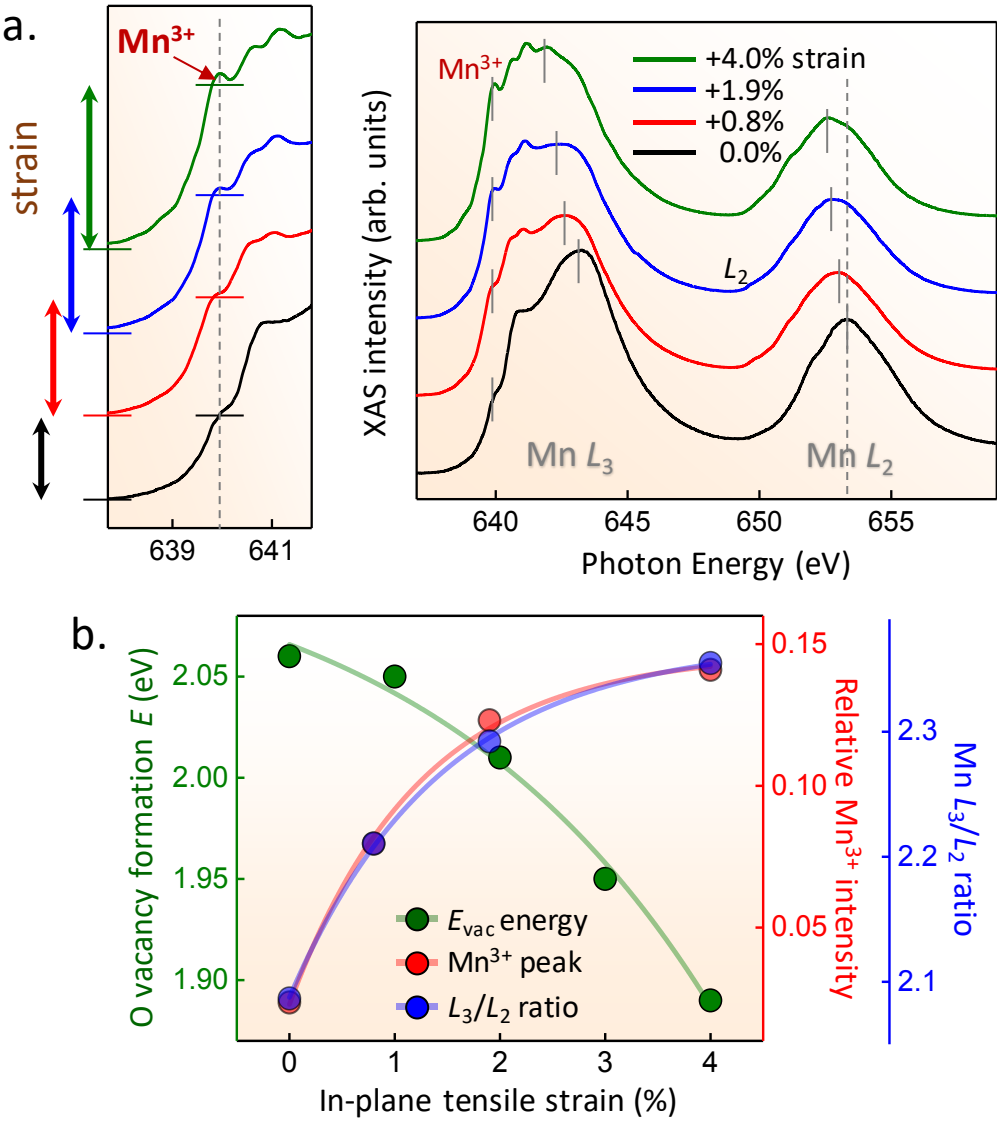


Figure 1. (a) Mn $L_{2,3}$ XAS spectroscopy of the strained ultra-thin CaMnO_3 films. Systematic evolution of the spectroscopic features at the Mn $L_{2,3}$ edges observed with substrate-induced tensile strain is consistent with the increase in the Mn^{3+} ion concentration induced by the oxygen vacancy formation. The key features include the chemical shift of the L_2 and L_3 spectral weights towards lower photon energies^{26, 27}, increase in the spectral weight of the Mn^{3+} high spin valence state

1
2
3 feature at approximately 640.3 eV (inset)^{31, 32}, and the growth of the L_3/L_2 ratio^{33, 34}. (b)
4
5 Experimental data (right axis) showing the continuous systematic variation of the Mn^{3+} feature
6
7 intensity as normalized to the total L_3 peak area (red markers), as well as the L_3/L_2 ratio (blue
8
9 markers) are correlated to the calculated strain-dependent oxygen vacancy formation energy (left
10
11 axis / green markers). Both the experimental and theoretical values are plotted as functions of in-
12
13 plane tensile strain.
14
15
16
17
18
19
20
21
22
23
24
25
26
27
28
29
30
31
32
33
34
35
36
37
38
39
40
41
42
43
44
45
46
47
48
49
50
51
52
53
54
55
56
57
58
59
60

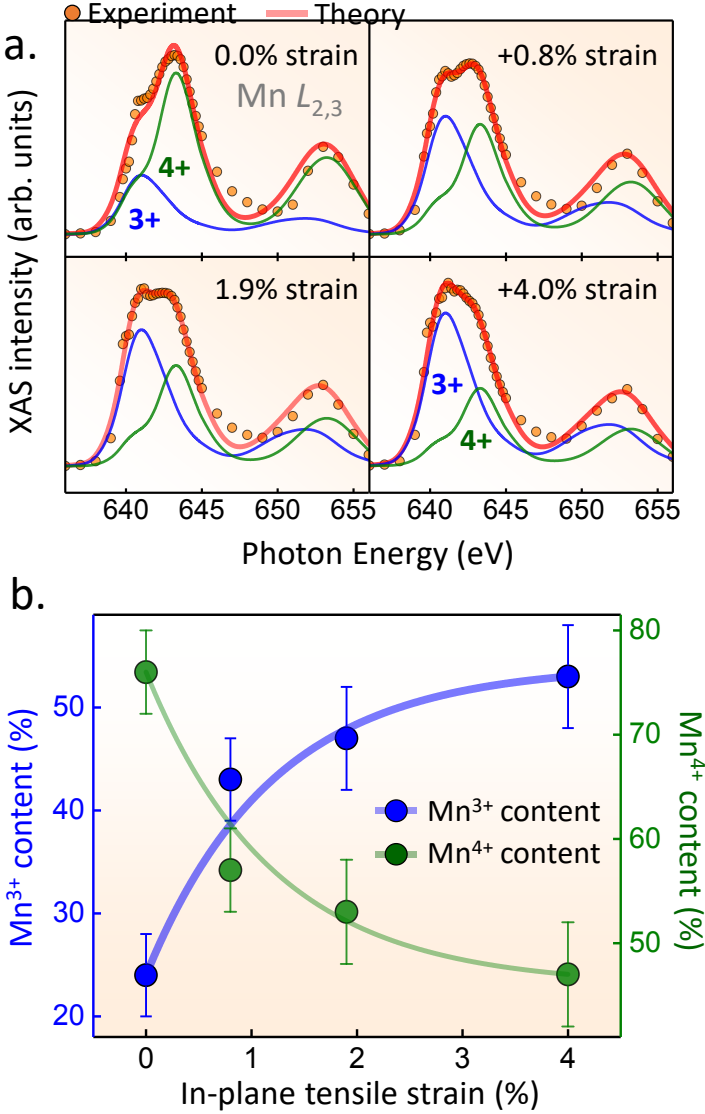


Figure 2. (a) Self-consistent simultaneous holistic fits of the strain-dependent experimental Mn $L_{2,3}$ edge spectra using the Mn³⁺ and Mn⁴⁺ spectral components obtained via atomic multiplet theoretical calculations⁴⁶. Resultant Mn³⁺ and Mn⁴⁺ ionic contents are plotted as a function of in-plane tensile strain in (b), and exhibit strain dependence similar to those of the experimental features shown in Figure 1b.

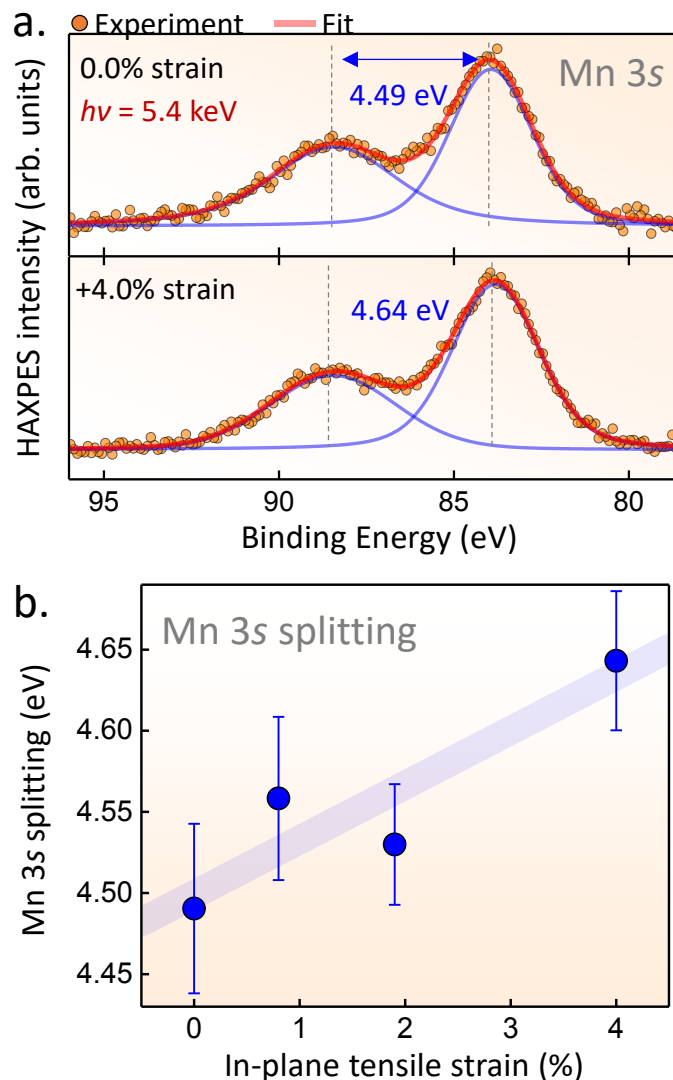


Figure 3. (a) Bulk-sensitive HAXPES of the Mn valence state in the CaMnO_3 buried layers. Mn 3s core-level spectra measured with the photon energy of 5.4 keV exhibit well-understood splitting due to the exchange coupling interaction³⁸. Magnitude of the splitting, quantified using self-consistent peak-fitting and shown for the fully relaxed (0% strain) and fully-strained (+4% strain) films, can be related to the mean valence state of the Mn ions in the film⁴⁰. (b) Magnitude of the Mn 3s peak splitting in the strained CaMnO_3 films plotted as a function of in-plane tensile strain exhibits a trend which suggests systematic increase in the Mn^{3+} ion content, consistent with the

result obtained via XAS spectroscopy as well as the calculations of oxygen vacancy formation energies.

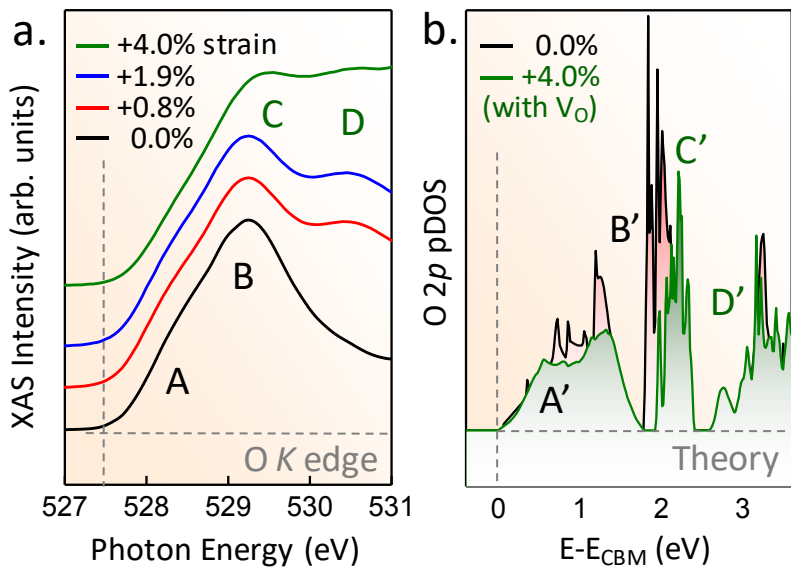


Figure 4. (a) XAS spectra of the O K pre-edge region shown for systematically varying in-plane tensile strain exhibit a lineshape evolution consistent with first-principles predicted changes in O 2p projected density-of-states shown in (b) (only one of the equivalent antiferromagnetic spin channels is shown). Peak positions and shifts calculated for the fully-relaxed and fully-strained films are in good agreement with the experimental data, with correspondences seen between features A–D in experiment and A'–D' in theory. States A' correspond to hybridized majority-spin Mn e_g – O 2p states, while B' and C' are hybridized minority-spin Mn t_{2g} – O 2p states that are shifted to higher energy with increasing strain. The defect state D' results from lowering of hybridized minority-spin Mn e_g – O 2p states adjacent to the vacancy.

Table of Contents Graphic

